Lawrence Berkeley National Laboratory
LBL Publications

Title

Lithium Tin Sulfide—a High-Refractive-Index 2D Material for Humidity-Responsive Photonic Crystals

Permalink

Journal

ISSN

Authors

Szendrei-Temesi, Katalin
Sanchez-Sobrado, Olalla
Betzler, Sophia B
et al.

Publication Date

2018-04-01

DOI

Peer reviewed

FULL PAPER

Humidity Sensors

ADVANCED
FUNCTIONAL
MATERIALS

www.afm-journal.de

Lithium Tin Sulfide—a High-Refractive-Index 2D Material for Humidity-Responsive Photonic Crystals

Katalin Szendrei-Temesi, Olalla Sanchez-Sobrado, Sophia B. Betzler,
*Katharina M. Durner, Tanja Holzmann, and Bettina V. Lotsch**

Extending the portfolio of novel stimuli-responsive, high-refractive-index (RI) materials besides titania is key to improve the optical quality and sensing performance of existing photonic devices. Herein, lithium tin sulfide (LTS) nanosheets are introduced as a novel solution processable ultrahigh RI material ($n = 2.50$), which can be casted into homogeneous thin films using wet-chemical deposition methods. Owing to its 2D morphology, thin films of LTS nanosheets are able to swell in response to changes of relative humidity. Integration of LTS nanosheets into Bragg stacks (BSs) based on TiO_2, SiO_2, nanoparticles or $H_3Sb_3P_2O_{14}$ nanosheets affords multilayer systems with high optical quality at an extremely low device thickness of below 1 µm. Owing to the ultrahigh RI of LTS nanosheets and the high transparency of the thin films, BSs based on porous titania as the low-RI material are realized for the first time, showing potential application in light-managing devices. Moreover, the highest RI contrast ever realized in BSs based on SiO_2 and LTS nanosheets is reported. Finally, exceptional swelling capability of an all-nanosheet BS based on LTS and $H_3Sb_3P_2O_{14}$ nanosheets is demonstrated, which bodes well for a new generation of humidity sensors with extremely high sensitivity.

1. Introduction

New materials solutions are key for the development of novel sensing platforms with improved optical properties and sensing performance compared to existing device concepts. One of the main challenges in the development of photonic sensors is to identify high-refractive-index (RI) materials which can easily be processed by wet-chemistry techniques and can be integrated into existing device architectures. In addition, for an effective application in sensor technology, these materials need to be stimuli responsive, which is typically achieved via inherent structural or textural porosity or swelling behavior in the presence of analytes.

The simplest photonic nanostructures used for optical sensing applications, which are capable of translating external stimuli into an optical signal by structural color changes, are 1D photonic crystals (1D PCs), also referred to as Bragg stacks (BSs).[1,2] BSs are composed of a high- and a low-RI material, which are stacked in an alternating fashion. The periodic modulation of the RIs creates a photonic stopband: a forbidden energy range for photons that are not allowed to propagate in the PC along certain directions in reciprocal space.[1] The photonic stopband defines the structural color and is dependent on the layer thickness d and the RI n of the constituent layers, given by the optical thickness $\tau = n \cdot d$.[3,4] By this means, dynamic variations in the layer thickness or in the RI induced by an analyte can be translated into changes in the stopband position and, hence, the structural color of the sensor.[5–12] The reflectance intensity—the intensity of the photonic stopband—is mostly defined by the RI contrast, i.e., the RI difference between the two materials.[2,3] Consequently, a high RI contrast results in devices with high reflectance intensities and better optical qualities featuring a lower overall device thickness of well below 1 µm.[13]

To create BSs with an ultrahigh RI contrast, high-RI materials are needed which preferably can be deposited via straightforward wet-chemical methods such as spin- or dip-coating. The most prominent candidate in the literature used as a high-RI material in BSs is titanium dioxide (TiO_2), which is applied either as a dense sol or as nanoparticles, forming a dense or a highly porous thin film, respectively.[4,14,15] Although sol–gel-based dense TiO_2 films or titania-based composite films have a maximum RI of around n (dense) = 2.12,[16–19] and n (composite) = 2.38,[20] respectively, volatile analytes cannot efficiently infiltrate the dense sol film, leading to significantly reduced or even inhibited vapor responsiveness.[16,17] On the

K. Szendrei-Temesi, Dr. S. B. Betzler, Dr. T. Holzmann, Prof. B. V. Lotsch
Nanochemistry Department
Max Planck Institute for Solid State Research
Heisenbergstraße 1, 70569 Stuttgart, Germany
E-mail: b.lotsch@fkf.mpg.de
K. Szendrei-Temesi, Dr. S. B. Betzler, K. M. Durner, Dr. T. Holzmann, Prof. B. V. Lotsch
Department of Chemistry
Ludwig-Maximilians-Universität (LMU)
Butenandtstraße 5-13, 81377 Munich, Germany
K. Szendrei-Temesi, Dr. S. B. Betzler, Dr. T. Holzmann, Prof. B. V. Lotsch
Nanosystems Initiative Munich (NIM) and Center for Nanoscience
Ludwig-Maximilians-Universität (LMU)
Schellingstraße 4, 80799 Munich, Germany
Dr. O. Sanchez-Sobrado
i3N/CENIMAT, Department of Materials Science
Faculty of Science and Technology
Universidade NOVA de Lisboa and CEMOP/UNINOVA
Campus de Caparica
2829516, Caparica, Portugal

The ORCID identification number(s) for the author(s) of this article can be found under https://doi.org/10.1002/adfm.201705740.

**ADVANCED
SCIENCE NEWS**
www.advancedsciencenews.com

**ADVANCED
FUNCTIONAL
MATERIALS**
www.afm-journal.de

contrary, nanoparticulate TiO_2 forms a highly porous thin film through textural porosity, and mesopore filling can be monitored by optical isotherms as a function of the relative pressure of the analyte.[7,16,21] Such porous TiO_2 layers exhibit an effective RI of $n = 1.70$–2.00, depending on the degree of porosity.[5,14,15] Combined with SiO_2 nanoparticles as the classical low-RI material, at least 10–12 layers are required to reach reflectance intensities of 90%, resulting in rather thick devices of several micrometers. A strategy to reduce the layer numbers and, hence, the device thickness, is the combination of highly porous SiO_2 with dense TiO_2 films.[17–19] Although a high RI contrast and good optical device quality were achieved, the sensitivity toward vapors is severely reduced due to the limited textural porosity of the titania layer. Another approach to increase the RI contrast is to identify new porous materials with a similar or even higher RI compared to TiO_2, although current alternatives such as WO_3 sol ($n = 2.03$),[22] ZrO_2 nanoparticles ($n = 1.70$),[23,24] Ta_2O_5[25] nanoparticles ($n = 1.80$), undoped or antimony-doped SnO_2 films (n (undoped) $= 1.83$, n (3% Sb-doped) $= 2.34$)[3,26] all feature lower RIs compared to dense titania or suffer from low transparency in the visible range. Thus, the highest RI contrast BSs reported so far combine highly porous silica layers stacked with dense titania layers, exhibiting an RI contrast of $\Delta n = 0.83$,[17] $\Delta n = 0.84$,[19] and $\Delta n = 0.89$.[18] To further increase the RI contrast is an important objective when aiming at high-quality optical devices, such as solar mirrors,[27] optical fibers,[28] or other light-managing devices.

All titania-based photonic structures employed for sensing feature textural porosity in order to facilitate analyte diffusion. However, to achieve high sensitivity toward analytes, swelling materials are preferred over porous materials as they cause larger stopband shifts via changes in their optical thickness.[6,12,29,30] Thus, the combination of two different swelling materials in one BS[31] is a promising strategy to induce ultralarge stopband shifts. To implement this strategy, the development of novel functional nanomaterials featuring both high swelling capability and high RI is one of the key challenges to be addressed.

Here, we present a new material platform for addressing both challenges: (i) we introduce a new solution processable high-RI material—lithium tin sulfide (LTS) nanosheets[32,33] ($n = 2.50$, 0% relative humidity (RH), 633 nm)—which forms high-quality BSs with TiO_2 as the low-RI material and produces ultrahigh RI contrast in PCs when combined with a low-RI material such as silica; and (ii) we demonstrate full-spectral color changes of

an all-nanosheet BS composed of LTS and antimony phosphate ($H_3Sb_3P_2O_{14}$) nanosheets. Taking advantage of the swelling capability of both 2D materials in the presence of water vapor, such stimuli-responsive all-nanosheet BSs are promising candidates for highly sensitive optical humidity sensors with good optical quality. The combination of two robust, swellable nanosheet materials ensures both high stability, especially compared to flexible organic materials, and presents a generic material platform that can be chemically tailored for diverse applications in chemo-optical sensing. In addition, the high RI contrast imparted by the inorganic nanosheets, combined with their high sensitivity to humidity, ensures superior optical quality combined with large signal changes, which makes LTS-based sensors competitive or even superior to other state-of-the-art optical sensors.[34,35]

2. Results and Discussion

2.1. Material Synthesis

Layered bulk lithium tin sulfide ($Li_2Sn_2S_5$) was synthesized by a classical solid-state reaction as previously described.[32] The successful synthesis was confirmed by powder X-ray diffraction (XRD) analysis, and the elemental composition was validated by energy-dispersive X-ray (EDX) and inductively coupled plasma (ICP) analysis, as shown in Figure S1 and Tables S1 and S2 in the Supporting Information. The crystal structure consists of covalent layers of edge sharing SnS_6 octahedra, whereby the Sn atoms are partially substituted by Li as depicted in **Figure 1**a.[33] The charge-compensating Li^+ ions are located in the interlayer gallery and allow for facile intercalation of water molecules between the covalent Sn(Li)S layers (Figure 2b). Spontaneous exfoliation in aqueous solution results in a stable colloidal suspension containing single nanosheets (Figure 1c) as demonstrated in the literature.[32] Upon drying, the stable suspensions of LTS nanosheets form thin films by random restacking of the single nanosheets in a turbostratically disordered fashion, as confirmed by the selected area electron diffraction (SAED) patterns (Figure S2, Supporting Information). Motivated by this film forming capability, spin-coating was explored to synthesize homogeneous thin films of exfoliated LTS nanosheets with a widely tunable thickness (see Figure S3 in the Supporting Information). The colloidal concentration was optimized to 60 mg mL^{-1}, which was sufficient to create homogeneous thin films with a thickness of around 20–40 nm (at 3000–5000 rpm
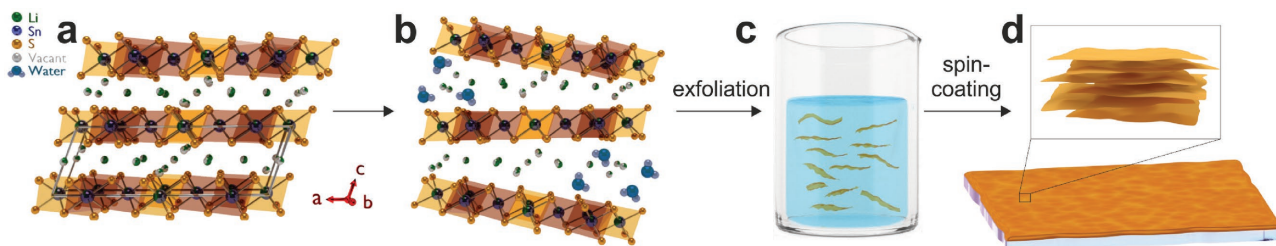
Figure 1. Thin film fabrication from colloidal suspensions of exfoliated LTS nanosheets. a) Crystal structure of layered bulk $Li_2Sn_2S_5$. b) Intercalation of water molecules into the interlayer space of $Li_2Sn_2S_5$. c) Spontaneous exfoliation of $Li_2Sn_2S_5$ into single-layered LTS nanosheets in water. d) Thin film fabrication starting from the stable colloidal suspension of single-layered LTS nanosheets via spin-coating.
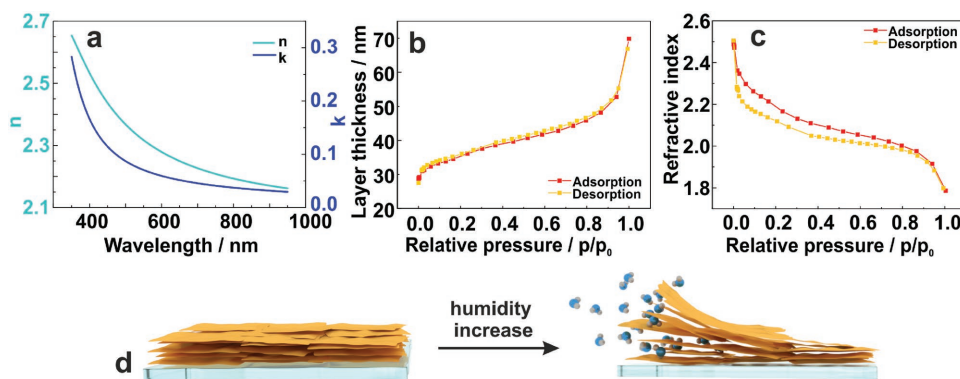
Figure 2. Optical properties of the fabricated LTS thin films. a) Wavelength-dependent n and k values for a LTS nanosheet film with a thickness of about 40 nm, measured under ambient conditions (30% RH). b) Layer thickness changes of an LTS film with changing partial pressure of water vapor, measured by ellipsometric porosimetry. c) RI changes with changing water vapor pressure in the atmosphere, measured by ellipsometric porosimetry. d) Scheme of the RH-dependent behavior of the LTS nanosheet thin films, showing the intercalation of ambient water molecules between the single nanosheets.

spin-coating speeds). The layer thickness can be fine-tuned by varying the number of the deposition steps and the spin-coating speed as further described in the Supporting Information.

2.2. Optical Properties of LTS Nanosheet Thin Films

In the first step, optical characterization of the LTS thin films was carried out as a basis for the optical design and rational tuning of the target photonic nanostructure. To this end, we studied homogeneous LTS nanosheet thin films via spectroscopic ellipsometry under ambient conditions ($\approx$30% RH) and with varying RH. In **Figure 2**a, the optical properties at ambient conditions (at $\approx$30% RH), the wavelength-dependent RI (n) and the extinction coefficient (k) of a 40 nm film are shown. As demonstrated in Figure 2a, the RI shows exceptionally high values, varying from $n = 2.65$ (at 350 nm, $\approx$30% RH) down to $n = 2.20$ (at 950 nm, $\approx$30% RH) with increasing wavelengths. The extinction coefficient was fitted to 0.30 at 400 nm, but decreases strongly and is below 0.10 in the range >450 nm. This small value indicates that thin films within this thickness range are essentially transparent, which is an important prerequisite for applying LTS as optical material in PCs. To test the response of LTS nanosheet films to humidity changes, the change of the optical properties with gradually increasing RH was monitored. According to Figure 2b, the layer thickness more than doubles (from 30 to 70 nm) throughout the entire humidity range (0–100% RH). As a second effect, the RI (at 633 nm) decreases with increasing humidity from $n = 2.50$ (0% RH) to $n = 1.75$ (100% RH), shown in Figure 2c. These two effects and the full reversibility as visible from the isotherms (Figure 2b,c) point to the facile intercalation of ambient water molecules between the nanosheets and subsequent swelling of the LTS film as shown in Figure 2d. While the effective layer thickness d increases as water intercalates between the nanosheets, the effective RI decreases through the increasing volume fraction of water ($n = 1.33$) contained in the pure nanosheets ($n = 2.50$, at 633 nm), thus leading to a significant response of the optical thickness ($\tau = n \cdot d$) to RH variations.

The remarkably high RI of the LTS nanosheets ($n = 2.50$) at 633 nm and 0% RH is significantly higher than the RI of dense ($n = 2.12$) or porous ($n = 1.70$–2.00, depending on the porosity) TiO_2 thin films. So far, TiO_2 with varying porosity has been most commonly used as the high-RI material in hierarchical photonic devices for vapor sensing.[8,10,21,36,37] However, due to only limited effective RI changes induced by the adsorption of analytes in the textural pores, only slight stopband shifts and, hence, generally low analyte sensitivity are observed.[17,21,38] In contrast, LTS nanosheet films show an even larger RI and significantly more pronounced swelling behavior, which is expected to give rise to greatly improved sensitivity in sensing applications.

To test this hypothesis and demonstrate the impact of the ultrahigh RI LTS material on the optical properties of the resulting PCs, we combine LTS nanosheet films with three different materials, namely TiO_2 nanoparticles, SiO_2 nanoparticles (Figure S4, Supporting Information), and $H_3Sb_3P_2O_{14}$ nanosheets.[11,39] We then characterize the resulting BSs regarding their structural and optical properties and investigate their behavior in terms of humidity sensing.

2.3. TiO₂ Nanoparticle and LTS Nanosheet-Based BS

The first photonic architecture we present is a BS built from LTS nanosheets and TiO_2 nanoparticles (**Figure 3**a). Owing to the high RI of LTS, this is the first reported multilayer structure where TiO_2 the lower RI. The scanning electron microscope (SEM) cross-sectional images displayed in Figure 3b,c show that the stacking of LTS nanosheets and TiO_2 nanoparticles in a periodic fashion was successful, leading to a highly homogeneous multilayer structure across large lateral dimensions on the micrometer range. The material contrast is clearly visible in the backscattered electron image (Figure 3b), where the LTS nanosheet layers appear brighter due to their higher atomic number (Z). The secondary electron images show two different morphologies, i.e., the sheet-like morphology for LTS and the particle nature of the TiO_2 nanoparticles (Figure 3c). The high stacking quality observed by SEM directly translates into excellent optical properties such as pronounced structural colors across large sample areas (Figure 3d) and high reflectance intensities (Figure 3e). The widely tunable structural color is

ADVANCED
SCIENCE NEWS
www.advancedsciencenews.com

ADVANCED
FUNCTIONAL
MATERIALS
www.afm-journal.de
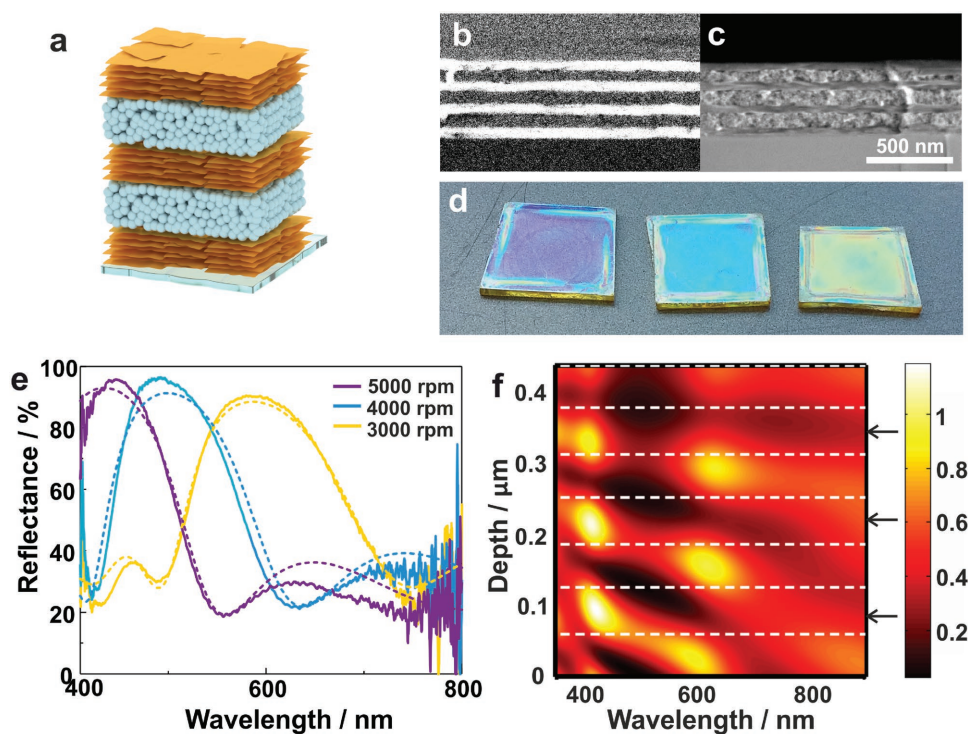
Figure 3. Optical properties of the TiO$_2$ nanoparticle/LTS nanosheet Bragg stacks. a) Scheme of the hybrid TiO$_2$ nanoparticle/LTS nanosheet Bragg stack. b) Backscattered and c) secondary electron SEM cross-sectional images of the fabricated samples, showing the homogeneous layered structure. d) Photographs of three samples consisting of seven layers on a glass substrate at ambient conditions, showing different structural colors caused by different layer thicknesses (the samples were spin-coated at 3000, 4000, and 5000 rpm rotation speed from left to right). The sample dimensions are 1.5 × 1.5 cm^2. e) Reflectance spectra (solid lines) and simulated spectra (dashed lines; Table S4, Supporting Information) of the three samples fabricated at different spin-coating speeds: 3000, 4000, and 5000 rpm. f) Spatial and spectral field distribution within the sample fabricated at 4000 rpm rotation speed, whereby the structure is shown in reverse, i.e., the substrate is located at 0.45 μm depth and the light source at 0 μm depth. The TiO$_2$ layers are indicated with arrows.

demonstrated in Figure 3d,e, whereby the different hues were accessed by applying different rotation speeds in the fabrication procedure via spin-coating, resulting in different layer thicknesses. The reflectance spectra in Figure 3e correspond to the devices shown in the photograph in Figure 3d and are composed of only seven layers on a glass substrate (LTS serving as the bottom and the top layer). This means that the RI contrast of LTS and TiO$_2$ is sufficiently high ($\Delta n = 0.40$ at ≈30% RH) to reach reflectance intensities over 90%. Simulations based on the transfer-matrix method[21] (Figure 3e, dashed spectra) confirm excellent agreement between the measured and the calculated spectra (for details, see Table S4 in the Supporting Information). Figure 3f depicts the calculated spectral and spatial field distribution within the BS (for the sample showing the blue structural color fabricated at 4000 rpm in Figure 3d), which is inhomogeneous throughout the photonic structure. We observe a field enhancement at the red stopband edge (≈600 nm), which is located in the LTS layers, and enhanced field intensities in the layers at the blue band edge region (≈400 nm) located in the TiO$_2$ layers. This again confirms that in this BS, TiO$_2$ serves as the low-RI material ($n = 1.80$ at 633 nm) for the first time, while the LTS nanosheets serve as the high-RI material ($n = 2.20$ at 30% RH, 633 nm). Maximizing the field intensities where TiO$_2$ has its maximum absorbance (around 370 nm) can be potentially useful for "slow photon" applications,[40,41] while

the combination of two high-RI materials allows for the creation of significantly thinner photonic structures (65–70% device thickness reduction compared to a SiO$_2$/LTS nanosheet BS containing only one high-RI material) and, hence, lower productions costs. Along similar lines, stopbands located in the IR range are more easily accessible, which may be useful, e.g., for applications in IR radiation shielding.

2.4. SiO$_2$ Nanoparticle and LTS Nanosheet-Based BSs

Motivated by the fact that LTS nanosheets are able to form high-quality BSs with TiO$_2$, we combined this ultrahigh RI material with SiO$_2$ nanoparticles ($n = 1.30$, **Figure 4**a; Figure S4, Supporting Information), which is the most commonly used low-RI material in PC research. The secondary electron and backscattered SEM images (Figure 4b,c) indicate homogeneous layering without intermixing and confirm the textural porosity of the nanoparticle layers, which provides accessibility to analytes. The well-defined photonic stopbands of different five-layer systems on glass substrates, along with their pronounced structural colors over a large area, viewed in reflectance, are shown in Figure 4d,f. The photograph row in Figure 4e was taken in transmission mode. The good visibility of the emblems below the glass substrate is a testament to the high transparency of
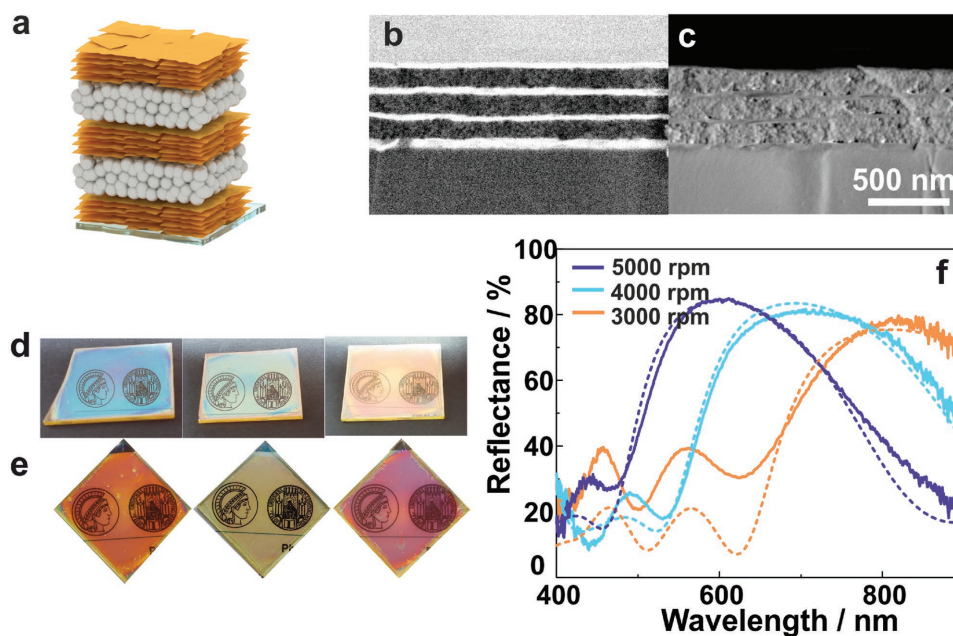
Figure 4. Optical properties of the SiO_2 nanoparticle/LTS nanosheet Bragg stacks. a) Schematic picture of the hybrid nanoparticle–nanosheet BS. b) Backscattered and c) secondary electron SEM cross-sectional image of an SiO_2 nanoparticle/LTS nanosheet BS containing seven layers. d) Photographs showing highly reflective samples, each based on five layers, with different structural colors caused by different layer thicknesses. e) Photographs taken in transmission mode demonstrate the high transparency of the samples. f) Reflectance spectra (solid lines) and simulated spectra (dashed lines) of the SiO_2 nanoparticles/LTS nanosheet BS containing five layers on a glass substrate. The samples were fabricated at different rotation speeds: 5000, 4000, and 3000 rpm, respectively.

the samples, while the structural colors are still pronounced and complementary to the reflection colors shown in Figure 4d.

According to Figure 4f, the reflectance spectra of the fabricated samples (Figure 4d,e) show high reflectance values of over 80% (for only five layers) and a bright Bragg peak with a peak width of ≈350 nm. This hybrid multilayer system has the highest RI contrast ($\Delta n = 0.90$ at 30% RH, 633 nm) that was reported in any BS to date (Figure 4a). The RI contrast value is even higher at lower RH values ($\Delta n = 1.20$ at 0% RH, 633 nm), as the RI of the LTS nanosheets strongly depends on the ambient water amount. So far, the highest RI contrasts found in BSs in the literature reach maximum values of $\Delta n = 0.83$,[17] $\Delta n = 0.84$,[19] and $\Delta n = 0.89$,[18] well below the RI contrast of our system. Comparing the experimental reflectance spectra with the simulated spectra (Figure 4f dashed lines, Table S5, Supporting Information) shows good agreement and confirms that the broad stopband arises from the superior RI contrast,[1] rather than from defects or other inhomogeneities. Increasing the number of layers above five resulted in more defects and more pronounced scattering, which is indicated by the higher reflectance minima (Figure S5, Supporting Information). Hence, for further studies, we use samples with five layers, as they already have a sufficiently high optical quality.

Next, we tested the humidity sensitivity of the SiO_2/LTS hybrid system, as the swelling behavior of the LTS layers, the high porosity of the SiO_2 layers, and the strong humidity-dependent RI variations indicate that this system is highly responsive to humidity variations. We observe two main effects, generated by RH changes (**Figure 5**a): (i) a stopband shift of 120 nm in the humidity range of 11–93% RH and (ii) continuously

decreasing reflectance intensities from 80% to 55% in this humidity range. Finally, at 100% RH, the stopband completely vanishes, i.e., the reflectance intensity is minimized (Figure 5a, darkest red spectrum). As shown by our calculations (Figure 5a, dashed line; Table S7, Supporting Information), this is due to the fact that the RIs of the two layer materials gradually become equal (11–93% RH) due to the water uptake, and at 100% RH, the RI contrast completely vanishes, turning the device transparent. The large stopband shifts and the transparency switching exhibit fast response (7.0 s) and recovery times (1.1 s) (Figure S11, Supporting Information), and are completely reversible for at least 15 cycles (Figure S9, Supporting Information). Upon RH decrease, the structural color and the photonic stopband reappear (Figure S12, Supporting Information). With this, we present the largest RI contrast in a BS, which is tunable and switchable due to environmental changes, i.e., changes in the humidity level.

2.5. $H_3Sb_3P_2O_{14}$ Nanosheet and LTS Nanosheet-Based BSs

To probe whether we can further increase the BS's sensitivity to humidity, we combine humidity-responsive LTS nanosheet films with films based on $H_3Sb_3P_2O_{14}$ nanosheets,[11,39,42,43] which have previously been reported to exhibit the largest response to ambient humidity ever recorded in a BS. Combining these two functional dielectrics into an all-swellable photonic architecture is expected to further increase the sensitivity of humidity as compared to existing devices.[11,12,44–46] The structure of the all-nanosheet 1D PCs, as depicted in **Figure 6**a,

**ADVANCED
SCIENCE NEWS**
www.advancedsciencenews.com

**ADVANCED
FUNCTIONAL
MATERIALS**
www.afm-journal.de
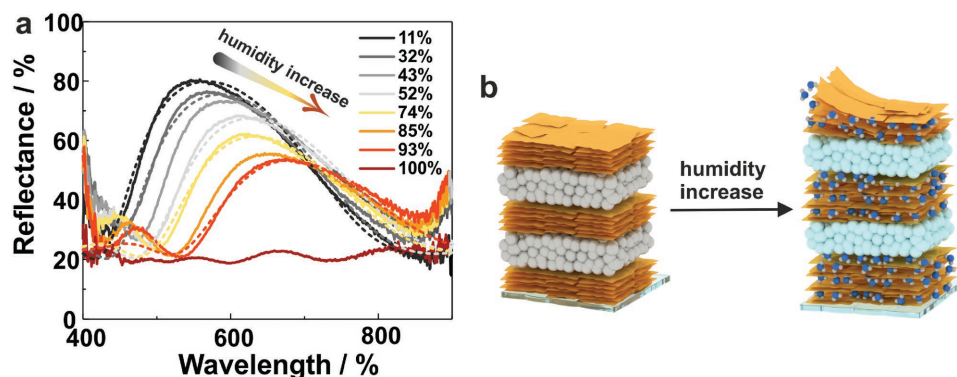
Figure 5. Humidity sensing properties of the SiO$_2$ nanoparticles/LTS nanosheet BSs. a) Measured (solid lines) and calculated (dashed lines) reflectance spectra of the SiO$_2$ nanoparticle/LTS nanosheet BS with changing RH. b) Proposed sensing mechanism based on the intercalation of water into the interlayer space of the LTS nanosheets and sorption of water in the textural pores of the SiO$_2$ nanoparticles.

is validated by the SEM cross-sectional image (Figure 6b) and shows the layered morphology with uniform layer stacking, low level of defects, and lateral homogeneity of the BS on the micrometer scale. However, since both materials exhibit a sheet-like morphology and similar atomic numbers (Z), their individual layer thicknesses cannot be determined by SEM. Likewise, EDX analysis cannot be used either as the signals of Sn and Sb appear at almost identical energies, prohibiting their distinction. Therefore, we applied electron energy loss spectroscopy (EELS) analysis in the transmission electron microscope (TEM) to differentiate the two materials at high spatial

resolution. H$_3$Sb$_3$P$_2$O$_{14}$ nanosheets show a dominant feature at 531.5 eV, which can be attributed to a superposition of the Sb–M$_{4,5}$ and the O–K edge. The EEL spectrum of LTS nanosheets exhibits the Sn–M$_{4,5}$ edge with an onset at 507.5 eV and a maximum at 536 eV (Figure S6, Supporting Information). Additionally, for LTS, we observe the S–L$_{2,3}$ edge with an onset at 166 eV. For both materials, an additional feature is visible at 686.5 eV in the spectra. This minor feature cannot be identified unequivocally and most likely originates from a contamination introduced by the focused ion beam (FIB) sample preparation. To extract the spatial distribution of the nanosheets across
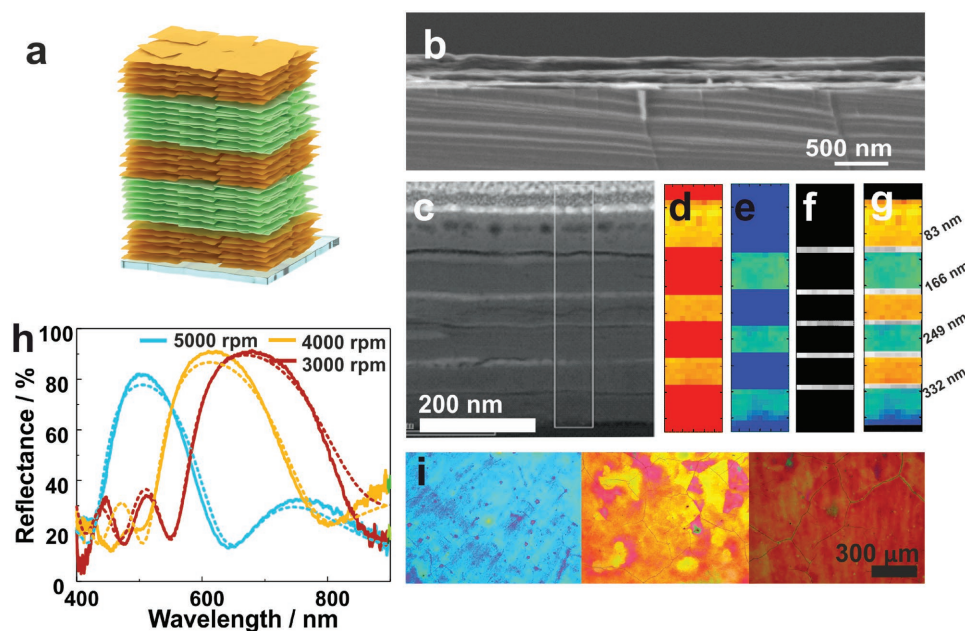
Figure 6. Architecture and structural properties of an all-nanosheet BS consisting of H$_3$Sb$_3$P$_2$O$_{14}$ nanosheets and LTS nanosheets. a) Schematic picture of the all-nanosheet BS deposited by spin-coating of the colloidal nanosheet suspensions. b) Secondary electron SEM cross-sectional image of the all-nanosheet BS showing the layered morphology across the entire sample and lateral homogeneity on the micrometer scale. c) TEM cross-sectional image of the all-nanosheet sample. The top layer appears to be thicker due to Ga and Pt integration caused by the FIB sample preparation. d) Electron energy loss (EEL) element mapping images taken from the sample area depicted in panel (c). d) Sn–M$_{4,5}$ edge. e) O–K and Sb–M$_{4,5}$ edges. f) The area, where all three edges (O–K, Sb–M$_{4,5}$ and Sb–M$_{4,5}$) are detected at the same time. g) Summarizing the element maps of all three edges. h) Reflectance spectra (solid lines) and simulated spectra (dashed lines) of three all-nanosheet BSs containing seven layers on a glass substrate at ambient conditions (30% RH). The different Bragg peak positions result from different rotation speeds in the spin-coating process: 5000, 4000, and 3000 rpm. i) Microscopic images depicting the different structural colors associated with the spectra shown in panel (h).

**ADVANCED
SCIENCE NEWS**
www.advancedsciencenews.com

**ADVANCED
FUNCTIONAL
MATERIALS**
www.afm-journal.de

the BS (TEM cross–sectional image shown in Figure 6c), the local EELS edge intensities were determined, and the resulting elemental distribution maps are depicted in Figure 6d–g. For experimental details, see the experimental section and Figures S6 and S7 in the Supporting Information. The EELS maps (Figure 6d,e) clearly confirm the layered morphology composed of alternating $H_3Sb_3P_2O_{14}$ and LTS layers with thicknesses of 50 ± 8 and 41 ± 8 nm, respectively. This alternating arrangement of the two different nanosheet materials is also confirmed by the mapping of the S–$L_{2,3}$ edge (Figure S7, Supporting Information), and is only found in the LTS nanosheet layer, yielding a thickness of 49 nm, which corresponds well to the layer thicknesses determined from the Sn edges. Additionally, the layer thicknesses were also confirmed by spectroscopic ellipsometry measurements at ambient conditions (Figure S8 and Table S3, Supporting Information). Hereby, the experimental data were fitted with a periodic model including three double layers on a silicon substrate. The layer thicknesses and the RIs were fitted to $d = 44$ nm and $n = 2.50$ (at 633 nm) for LTS and $d = 62$ nm and $n = 1.56$ (at 633 nm) for $H_3Sb_3P_2O_{14}$ at ambient RH, which is in excellent agreement with the EELS element mapping data. According to Figure 6h, the homogeneously stacked layered structure is also confirmed by the high reflectance intensities of the Bragg peak, created by the alternating arrangement of seven layers of LTS and $H_3Sb_3P_2O_{14}$ nanosheets on a glass substrate, terminated by a top layer of LTS nanosheets. By changing the spin-coating speeds and the layer thicknesses within the stack, different structural colors are accessible all over the visible spectral range (Figure 6h,i). Simulations of the reflectance spectra (Figure 6h, dashed lines; Table S6, Supporting Information) based on the RIs extracted by ellipsometric porosimetry confirm the layer thicknesses determined by the EELS mapping.

As shown in Figure 6h, seven alternating layers of the two nanosheet materials with an RI contrast of $\Delta n = 0.65$ are sufficient to obtain reflectance intensities of ≈90%. This allows for the fabrication of ultrathin photonic structures with good optical quality, as only a few layers are needed to reach high reflectance values.

Given the observed swelling capability of both individual nanosheet materials in the presence of water,[11] we tested the humidity sensing performance of the all-nanosheet photonic structure. As shown in **Figure 7**a,b, the all-nanosheet stack shows a significant color change (in the range of 11–93% RH), larger than for any other photonic system reported for humidity sensing applications so far.[11,46,47] In the range of 11–93% RH (Figure 4c), a stopband shift of 140 nm is observed (Figure 4a,b), resulting in a very high sensitivity of 1.54 nm per percent of analyte, which is larger compared to BSs, which contain only one swelling compound (see above and previous works).[11,12] The high sensitivity combined with fast response (9.2 s) and recovery times (2.4 s) (Figure S11, Supporting Information) makes these optical sensors competitive or even superior to other existing devices. Notably, the stopband redshifts nearly linearly with increasing RH values, which is highly desirable for sensing applications (Figure 7b). The excellent agreement between the performed theoretical calculations (Figure 7a, dashed lines; Table S8, Supporting Information) and the measured spectra (Figure 7a, solid lines) indicates that the large stopband shifts arise from ≈50% swelling for the LTS nanosheets and ≈60% swelling for $H_3Sb_3P_2O_{14}$ due to water intercalation (Figure 7d). In addition, a gradual decrease in the RI contrast upon water intercalation is noticeable by changes in the reflectance intensity from 95% to 60% in the RH range of 11–93%, induced by the water uptake (Table S8, Supporting
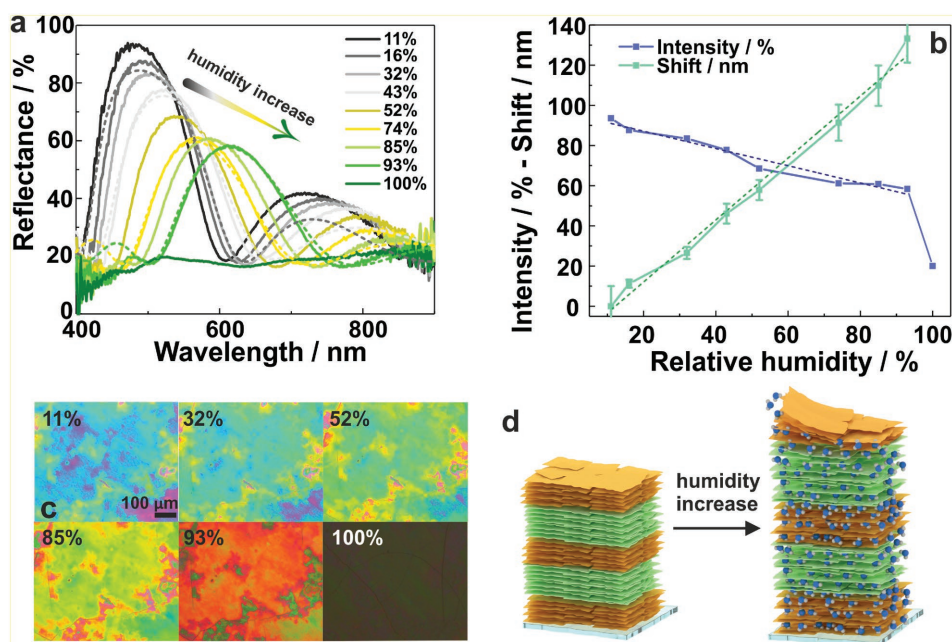
Figure 7. Humidity-dependent behavior of the all-nanosheet BS. a) Humidity-dependent reflectance spectra (solid lines) and simulated spectra (dashed lines) taken at different RH values. b) Humidity-dependent stopband shifts and reflectance intensity maximum changes of the all-nanosheet sample with increasing RH. c) Series of microscope images taken at different RH values showing the different structural colors. d) Schematic illustration of the proposed sensing mechanism, i.e., the swelling of both nanosheet materials by water intercalation into the interlayer space.

Information). Both materials take up water, leading to reduced effective RIs of n (LTS) = 1.78 and n ($H_3Sb_3P_2O_{14}$) = 1.52 at 93% RH, respectively, ranging between those of the pure materials and water.[11] We further find that the intercalation of water has a higher impact on the RI of the LTS nanosheets, which changes by $\Delta n = 0.72$ as compared to that of the $H_3Sb_3P_2O_{14}$ nanosheets, $\Delta n = 0.08$ (Table S8, Supporting Information). This effect can most likely be traced back to the significantly higher initial RI of the LTS nanosheets, whereby the intercalation of water causes larger changes in the effective RI of the thin films compared to the $H_3Sb_3P_2O_{14}$ nanosheets, which exhibit an initial RI more similar to water ($n = 1.33$). Between 93% and 100% RH, the reflectance intensity further decreases and, finally, the RI contrast is fully compensated and the stopband completely vanishes, such that the BS appears transparent (i.e., dark in the reflection mode, Figure 7d, 100% RH). This effect of reversible transparency switching is a rare phenomenon and was observed only for very few systems so far, as a careful material choice and adjustment of structural and dielectric parameters is required.[11,48] Since water intercalation happens at equilibrium, the structural color and the photonic stopband can be restored with decreasing humidity. The observed ultralarge stopband shifts as well as the transparency switching (Figure S12, Supporting Information) are fully reversible, and the sensor is stable for at least ten cycles (10–95% RH) of humidity increase and decrease (Figure S10, Supporting Information).

3. Conclusion

In summary, we have introduced LTS nanosheets as a solution processable novel high-refractive-index material ($n = 2.50$ at 0% RH at 633 nm), which, owing to its nanosheet morphology and excellent film-forming properties, lends itself well as constituent material for the fabrication of ultrathin, high optical contrast photonic nanostructures. We have demonstrated the first PC featuring TiO_2 as low-index material, and achieved the highest refractive index contrast in SiO_2 nanoparticle—LTS nanosheet Bragg stacks ($\Delta n = 1.20$ at 0% RH, 633 nm, $\Delta n = 0.90$ at 30% RH) reported to date. The high RI of LTS nanosheets offers enhanced flexibility in the creation of novel light-managing devices, such as antireflection coatings, optical waveguides, solar cells, solar mirrors, displays, or ophthalmic devices. Another field of interest relates to titania-based photonic nanostructures where both maximum electric field concentration and absorption of TiO_2 can be tuned into the UV range for "slow photon" applications. In addition, combining two high-RI materials in a BS can lead to a significant reduction in device thickness and with it, material and cost efficiency. This effect could be exploited, for example, for devices used in radiation shielding, with a photonic stopband placed in the IR spectral range. We have further demonstrated the first all-nanosheet Bragg stacks composed of LTS and antimony phosphate, $H_3Sb_3P_2O_{14}$, nanosheets, which are both able to take up significant amounts of water into their interlayer space. Upon exposure to ambient humidity, we observe a full-spectral, linear stopband shift with increasing relative humidity between 11% and 93% RH, which is fully reversible. Notably, due to the high RI contrast, we achieve reflectance intensities above 90% (at

10% RH) for a device consisting of only seven layers (<1 µm) in total. This novel BS architecture, therefore, presents an ultra-sensitive colorimetric humidity sensor entirely based on functional 2D materials, which, more generally, constitutes a generic material platform for the detection of a variety of analytes.

4. Experimental Section

Material Synthesis: Bulk $Li_2Sn_2S_5$ was synthesized via a one-step solid state synthesis.[32] The precursors, Li_2S, Sn, and S, were stoichiometrically mixed under inert gas atmosphere, filled into a glassy carbon crucible, and vacuum-sealed in a quartz tube. A slight excess of sulfur (3 wt%) was applied in order to ensure the complete oxidation of Sn. The tubes were heated to 750 °C with a ramp of 1 °C min^{-1} for 48 h and subsequently quenched to room temperature.

$K_3Sb_3P_2O_{14}$ was also synthesized by a solid state reaction as described elsewhere.[11] For protonation, 4 g of the resulting white powder was stirred in 250 mL of 8 M HNO_3 overnight and washed with pure water. To ensure complete protonation, this step was repeated once again.

Preparation of Colloidal Suspensions: For exfoliation, the bulk $Li_2Sn_2S_5$ was shaken in water for several hours with a concentration of 1 g L^{-1}. To ensure complete exfoliation, the suspension was sonicated for 60 min. To collect the exfoliated nanosheets, the suspension was centrifuged at 24 000 rpm for 30 min. The brownish pellet was resuspended in a water–ethanol mixture (60 vol% ethanol) with a concentration of 60 mg mL^{-1}. Afterward, the suspension was sonicated for 2 h before using it in the BS fabrication.

The bulk $H_3Sb_3P_2O_{14}$ was exfoliated likewise by stirring the protonated compound in pure water overnight. The suspension was centrifuged first at 3000 rpm to get rid of the non-exfoliated residual bulk and then at 18 000 rpm to obtain the nanosheets. The gel-like pellet was dried at 100 °C and resuspended in a water–ethanol mixture (60 vol% ethanol) with a concentration of 27.5 mg mL^{-1}. This suspension was sonicated 2 h before spin-coating.

TiO_2 was synthesized by hydrolysis of $Ti(OEt)_4$ in diluted acid.[9] Here, 12.5 mL tetraethylorthotitanate (Sigma Aldrich) was added dropwise under vigorous stirring to 75 mL of 0.1 M HNO_3 and heated at 80 °C for 8 h. The white suspension was sonicated for 3 h and washed three times by centrifuging the particles at 24 000 rpm and redispersing the pellet in methanol. A final concentration of 3 wt% was used for spin-coating.

Colloidal SiO_2 (LUDOX, SigmaAldrich) was diluted with methanol to 3.2 wt% and after 10 min sonication, directly used for spin-coating.

Bragg Stack Preparation: All BSs were prepared by spin-coating (WS-650S-NPP-Lite, Laurell Technologies Corporation) using the stable colloidal suspensions with the concentrations given above. To access different film thicknesses and, hence, structural colors, different spin-coating speeds and the number of deposition steps were varied. Here, 150 µL of the colloidal suspensions were spin-coated alternately on plasma-cleaned glass substrates (1.5 cm × 1.5 cm) for 1 min with defined speeds (3000, 4000, and 5000 rpm) and with an acceleration of 7000 rpm s^{-1}. The first layer on top of the glass substrate and also the last one were the LTS nanosheets to achieve the highest achievable RI contrast at the interfaces. To create one layer within the Bragg stack, LTS was deposited for all samples in two steps, and the samples were heated after each deposition step to 80 °C for 15 min in order to stabilize the layers and to get rid of the residual solvents.

Characterization: SEM images of the LTS bulk material and the EDX analysis to verify the S:Sn ratio was performed on an FEI Helios G3 UC SEM. In addition, ICP measurements were performed on a Varian Vista RL. XRD patterns were recorded on a powder X-ray diffractometer (Stadi P, STOE) working with Ge(111) monochromated Mo Kα1 radiation (λ = 70.926 pm) and a Mythen 1K detector (Dektris). The crystalline nanosheet compounds were identified by comparing the powder diffraction patterns of the bulk materials.[32,49] Cross-sectional images of the BSs were taken with a Zeiss Gemini Ultra Field Emission SEM. For the TEM measurement, the sample was cut via FIB (Zeiss 1540EsB) with

**ADVANCED
SCIENCE NEWS**

www.advancedsciencenews.com

**ADVANCED
FUNCTIONAL
MATERIALS**

www.afm-journal.de

a 30 kV Ga ion beam, and the surface was polished with a 3 kV beam. The TEM cross-sectional measurement was performed on an FEI Titan Themis microscope 60–300 kV equipped with a Cs corrector for the probe at 300 kV. EELS investigations were performed in scanning transmission mode with a convergence semiangle of 16.6 mrad and an energy resolution of 0.75 eV. To reduce the effect of the electron irradiation on the material, subpixel scanning was applied during the spectrum image acquisition. The EELS maps for the spectral region of 100–612.25 eV were generated by integrating the intensity of background-corrected spectra in defined energy windows. The background was subtracted by performing a power-law fit for an energy width of 60 eV starting from 429 eV for the Sn–$M_{4,5}$ edge and from 467 eV for the Sb–$M_{4,5}$/O–K edge. Subsequently, the intensity of the edges was integrated in an energy window of 100 eV starting at 507.5 eV for the Sn–$M_{4,5}$ and at 530.5 eV for the Sb–$M_{4,5}$/O–K edge. The same procedure was used to generate the intensity map of the S–$L_{2,3}$ edge, but in that case the background was corrected by a power-law fit in the spectral range of 130.25–160.25 eV and the intensity was integrated between 161 and 216 eV.

Ellipsometric porosimetry measurements on the thin films were carried out by the porosimetry tool of a Sopra PS-1000 ellipsometer, whereby the samples were equilibrated at selected partial pressure values of water vapor for 15 min. The measured spectra were fitted with the software Sopra SAE using the model combination Cauchy and Lorentz. For the nanosheet thin films, both the layer thickness and the RI were fitted over the relative pressure range simultaneously.

Microscope images were taken from the BS surface with an optical microscope (DM2500, Leica) and simultaneously reflectance spectra were measured at normal incidence with a fiber optic spectrometer (USB2000+, Ocean Optics) attached to the microscope.

To monitor the optical changes with changes in RH, the BSs were kept in a closed stainless steel chamber with a total volume of 5 mL and with a transparent glass window. In the chamber, 0.7 mL of saturated salt solutions was filled without touching the sample surface and kept at 25 °C to define the humidity in the closed atmosphere.[50,51] At each step, 20 min equilibration time was needed. Dynamic cycling measurements between 10% and 95% RH were performed using a nitrogen flow setup.

Simulations: Numerical calculations of the reflectance spectra were carried out with a Matlab code based on a full-vector calculation using the transfer matrix method as reported elsewhere.[21] The layer thicknesses at 0% RH were taken from the SEM cross-sectional images. The (wavelength-dependent) RIs were taken from the porosimetry measurements.

Supporting Information

Supporting Information is available from the Wiley Online Library or from the author.

Acknowledgements

Conflict of Interest

The authors declare no conflict of interest.

[1] J. D. Joannopoulos, S. G. Johnson, J. N. Winn, R. D. Meade, *Photonic Crystals: Molding the Flow of Light*, Princeton University Press, Princeton, NJ, USA **2008**.

[2] J. D. Joannopoulos, P. R. Villeneuve, S. Fan, *Nature* **1997**, *386*, 143.

[3] L. D. Bonifacio, B. V. Lotsch, D. P. Puzzo, F. Scotognella, G. A. Ozin, *Adv. Mater.* **2009**, *21*, 1641.

[4] S. Colodrero, M. Ocaña, H. Míguez, *Langmuir* **2008**, *24*, 4430.

[5] S. Colodrero, M. Ocana, A. R. Gonzalez-Elipe, H. Miguez, *Langmuir* **2008**, *24*, 9135.

[6] B. V. Lotsch, G. A. Ozin, *ACS Nano* **2008**, *2*, 2065.

[7] S. Y. Choi, M. Mamak, G. von Freymann, N. Chopra, G. A. Ozin, *Nano Lett.* **2006**, *6*, 2456.

[8] A. Ranft, F. Niekiel, I. Pavlichenko, N. Stock, B. V. Lotsch, *Chem. Mater.* **2015**, *27*, 1961.

[9] F. M. Hinterholzinger, A. Ranft, J. M. Feckl, B. Ruhle, T. Bein, B. V. Lotsch, *J. Mater. Chem.* **2012**, *22*, 10356.

[10] I. Pavlichenko, E. Broda, Y. Fukuda, K. Szendrei, A. K. Hatz, G. Scarpa, P. Lugli, C. Brauchle, B. V. Lotsch, *Mater. Horiz.* **2015**, *2*, 299.

[11] K. Szendrei, P. Ganter, O. Sànchez-Sobrado, R. Eger, A. Kuhn, B. V. Lotsch, *Adv. Mater.* **2015**, *27*, 6341.

[12] P. Ganter, K. Szendrei, B. V. Lotsch, *Adv. Mater.* **2016**, *28*, 7294.

[13] M. Anaya, J. P. Correa-Baena, G. Lozano, M. Saliba, P. Anguita, B. Roose, A. Abate, U. Steiner, M. Gratzel, M. E. Calvo, A. Hagfeldt, H. Miguez, *J. Mater. Chem. A* **2016**, *4*, 11214.

[14] J. J. Steele, A. C. van Popta, M. M. Hawkeye, J. C. Sit, M. J. Brett, *Sens. Actuators, B* **2006**, *120*, 213.

[15] M. M. Hawkeye, M. J. Brett, *Adv. Funct. Mater.* **2011**, *21*, 3652.

[16] N. Hidalgo, M. E. Calvo, H. Míguez, *Small* **2009**, *5*, 2309.

[17] M. Anaya, A. Rubino, M. E. Calvo, H. Miguez, *J. Mater. Chem. C* **2016**, *4*, 4532.

[18] W. J. Nimens, L. Whittaker-Brooks, M. H. Bartl, *J. Mater. Chem. C* **2016**, *4*, 668.

[19] B. Brudieu, A. L. Bris, J. Teisseire, F. Guillemot, G. Dantelle, S. Misra, P. R. i. Cabarrocas, F. Sorin, T. Gacoin, *Adv. Opt. Mater.* **2014**, *2*, 1105.

[20] J. L. H. Chau, Y.-M. Lin, A.-K. Li, W.-F. Su, K.-S. Chang, S. L.-C. Hsu, T.-L. Li, *Mater. Lett.* **2007**, *61*, 2908.

[21] M. C. Fuertes, S. Colodrero, G. Lozano, A. R. González-Elipe, D. Grosso, C. Boissière, C. Sánchez, G. J. d. A. A. Soler-Illia, H. Míguez, *J. Phys. Chem. C* **2008**, *112*, 3157.

[22] E. Redel, C. Huai, M. Renner, G. von Freymann, G. A. Ozin, *Small* **2011**, *7*, 3465.

[23] M. E. Calvo, J. R. Castro Smirnov, H. Míguez, *J. Polym. Sci., Part B: Polym. Phys.* **2012**, *50*, 945.

[24] J. R. C. Smirnov, M. Ito, M. E. Calvo, C. López-López, A. Jiménez-Solano, J. F. Galisteo-López, P. Zavala-Rivera, K. Tanaka, E. Sivaniah, H. Míguez, *Adv. Opt. Mater.* **2015**, *3*, 1633.

[25] B. Gospodinov, J. Dikova, S. Mintova, T. Babeva, *J. Phys.: Conf. Ser.* **2012**, *398*, 012026.

[26] S. Gürakar, T. Serin, N. Serin, *Appl. Surf. Sci.* **2015**, *352*, 16.

[27] A. Jiménez-Solano, M. Anaya, M. E. Calvo, M. Alcon-Camas, C. Alcañiz, E. Guillén, N. Martínez, M. Gallas, T. Preussner, R. Escobar-Galindo, H. Míguez, *Adv. Opt. Mater.* **2017**, *5*, 1600833.

[28] C. Bariáin, I. R. Matı as, F. J. Arregui, M. López-Amo, *Sens. Actuators, B* **2000**, *69*, 127.

[29] B. V. Lotsch, G. A. Ozin, *Adv. Mater.* **2008**, *20*, 4079.

[30] Z. Wang, J. Zhang, J. Xie, C. Li, Y. Li, S. Liang, Z. Tian, T. Wang, H. Zhang, H. Li, W. Xu, B. Yang, *Adv. Funct. Mater.* **2010**, *20*, 3784.

[31] B. V. Lotsch, G. A. Ozin, *J. Am. Chem. Soc.* **2008**, *130*, 15252.

[32] A. Kuhn, T. Holzmann, J. Nuss, B. V. Lotsch, *J. Mater. Chem. A* **2014**, *2*, 6100.

[33] T. Holzmann, L. M. Schoop, M. N. Ali, I. Moudrakovski, G. Gregori, J. Maier, R. J. Cava, B. V. Lotsch, *Energy Environ. Sci.* **2016**, *9*, 2578.

[34] H. S. Jung, P. Verwilst, W. Y. Kim, J. S. Kim, *Chem. Soc. Rev.* **2016**, *45*, 1242.

[35] S. Sikarwar, B. C. Yadav, *Sens. Actuators, A* **2015**, *233*, 54.

[36] G. von Freymann, V. Kitaev, B. V. Lotsch, G. A. Ozin, *Chem. Soc. Rev.* **2013**, *42*, 2528.

[37] A. T. Exner, I. Pavlichenko, B. V. Lotsch, G. Scarpa, P. Lugli, *ACS Appl. Mater. Interfaces* **2013**, *5*, 1575.

[38] A. Ranft, I. Pavlichenko, K. Szendrei, P. M. Zehetmaier, Y. Hu, A. von Mankowski, B. V. Lotsch, *Microporous Mesoporous Mater.* **2015**, *216*, 216.

[39] Y. Piffard, A. Verbaere, A. Lachgar, S. Deniard-Courant, M. Tournoux, *Rev. Chim. Miner.* **1986**, *23*, 766.

[40] J. I. L. Chen, G. von Freymann, S. Y. Choi, V. Kitaev, G. A. Ozin, *Adv. Mater.* **2006**, *18*, 1915.

[41] T. Baba, *Nat. Photonics* **2008**, *2*, 465.

[42] J.-C. P. Gabriel, F. Camerel, B. J. Lemalre, H. Desvaux, P. Davidson, P. Batail, *Nature* **2001**, *413*, 504.

[43] S. Deniard-Courant, Y. Piffard, P. Barboux, J. Livage, *Solid State Ionics* **1988**, *27*, 189.

[44] C.-Y. Lee, G.-B. Lee, *Sens. Lett.* **2005**, *3*, 1.

[45] R. A. Barry, P. Wiltzius, *Langmuir* **2005**, *22*, 1369.

[46] E. Tian, J. Wang, Y. Zheng, Y. Song, L. Jiang, D. Zhu, *J. Mater. Chem.* **2008**, *18*, 1116.

[47] R. Xuan, Q. Wu, Y. Yin, J. Ge, *J. Mater. Chem.* **2011**, *21*, 3672.

[48] M. N. Ghazzal, O. Deparis, J. De Coninck, E. M. Gaigneaux, *J. Mater. Chem. C* **2013**, *1*, 6202.

[49] Y. Piffard, A. Lachgar, M. Tournoux, *J. Solid State Chem.* **1985**, *58*, 253.

[50] P. W. Winston, D. H. Bates, *Ecology* **1960**, *41*, 232.

[51] L. Greenspan, *J. Res. Nat. Bur. Stand.* **1977**, *81A*, 89.